Corrosion Science 196 (2022) 110048

Contents lists available at ScienceDirect

Corrosion Science

journal homepage: www.elsevier.com/locate/corsci

Insights into the roles of intergranular carbides in the initiation of intergranular stress corrosion cracking of alloy 690 in simulated PWR primary water

Wenjun Kuang [a,*], Xingyu Feng [a], Han Yue [a], Gary S. Was [b], Xianchao Hao [c,d]

[a] Center for Advancing Materials Performance from the Nanoscale (CAMP-Nano), State Key Laboratory for Mechanical Behavior of Materials, Xi'an Jiaotong University, Xi'an 710049, PR China

[b] Department of Nuclear Engineering and Radiological Sciences, University of Michigan, Ann Arbor, MI 48109, United States

[c] CAS Key Laboratory of Nuclear Materials and Safety Assessment, Institute of Metal Research, Chinese Academy of Sciences, Shenyang 110016, China

[d] Shi-changxu Innovation Center for Advanced Materials, Institute of Metal Research, ChineseAcademy of Sciences, Shenyang 110016,China

ARTICLE INFO

Keywords:
Alloy
STEM
Oxidation
Intergranular corrosion
Stress corrosion

ABSTRACT

The effect of intergranular carbides on the stress corrosion crack (SCC) initiation of alloy 690 in high-temperature hydrogenated water was systematically studied. Irrespective of the aging temperature, the resistance to SCC initiation continuously increases with increasing carbide coverage. The understanding of carbide effects was further advanced. Mechanically, the carbide mitigates the breach of surface oxide film over the grain boundary by suppressing the local apparent plastic strain. The carbide also greatly diminishes grain boundary migration by retarding the diffusion of Cr. More importantly, it decomposes when exposed to the environment and serves as Cr source for forming protective oxide film.

1. Introduction

Alloy 690 is one of the key structure materials in nuclear power plants. It possesses higher stress corrosion cracking (SCC) resistance than its predecessor alloy 600 and is widely used as heat transfer tubes in pressurized water reactor (PWRs) steam generators. No cracking incident has been reported in this alloy in the field thus far. It was found that the high resistance to SCC initiation of alloy 690 in simulated PWR primary environment is linked to its tendency to form a compact Cr-rich oxide film over the random high angle grain boundary which impedes the further ingress of oxygen along the grain boundary [1–6]. Nevertheless, SCC initiation still occurs on this alloy under dynamic straining condition once the surface protective oxide film is breached and intergranular oxidation ensues, as outlined in the previous works [7,8]. The detailed characterization of the SCC cracks on solution-annealed alloy 690 shows that grain boundary migration and intergranular oxidation are two fundamental steps in the SCC process of this alloy [8,9]. Those works improved our understanding of the SCC initiation behavior of alloy 690 in PWR primary water environment. However, the role of intergranular carbides, which are important microstructural features in the SCC initiation process, has not been fully addressed yet.

Ni-base alloys are normally thermally treated (TT) prior to application as the semi-continuous intergranular carbides that form on grain boundaries were found to enhance their resistance to SCC initiation of both alloy 600 [10–12] and alloy 690 [13,14] in reducing environments. Although some works have been conducted to clarify the mitigation mechanism of intergranular carbide in the SCC of alloy 600, the underlying mechanism is still not universally accepted. An early theory proposed by Bruemmer et al. [15] was that the beneficial effect of carbide was due to its ability to blunt a crack through its role as a dislocation source. More recent works [16–20] suggest that the intergranular carbide could serve as a source of Cr for the formation of Cr-rich oxides and grain boundary pinning, contributing to the suppression of intergranular oxidation and grain boundary migration in simulated PWR primary water or high temperature hydrogenated steam. However, the relevant work on alloy 690 is still very limited and the manner in which intergranular carbides affect grain boundary degradation processes in alloy 690 is still debatable.

The results from U-bend tests [13] and constant extension rate tensile (CERT) tests [14] suggest that intergranular carbides can enhance the resistance to SCC initiation of alloy 690 in both caustic and simulated PWR primary water. However, some results indicate that the effect of

* Corresponding author.
E-mail address: wjkuang66@gmail.com (W. Kuang).

https://doi.org/10.1016/j.corsci.2021.110048
Received 17 October 2021; Received in revised form 21 December 2021; Accepted 22 December 2021
Available online 27 December 2021

Table 1
The experimental conditions and SCC initiation results of the CERT tests in 360 °C water containing 18 cm^3 (STP) H_2/kg H_2O.

Material Designation	Yield strength (MPa)	Uniform strain (%)	Test duration (h)	Average crack length (μm)	Crack number density (mm^{-2})	Crack length per unit area (μm/mm^2)
SA-00–00	189	1.78	564	4.1 ± 0.3	11.4 ± 7.4	46.8 ± 30.7
		3.39	1391	9.8 ± 0.1	106.6 ± 27.2	1042.1 ± 266.0
SA-475–10000	204	3.44	1391	9.9 ± 0.2	44.9 ± 14.3	444.6 ± 141.3
SA-550–10000	179	3.51	1391	7.7 ± 0.3	27.1 ± 14.1	208.3 ± 108.4
SA-700–17	205	1.63	564	None	None	None
		3.43	1391	2.5 ± 0.5	10.2 ± 9.9	25.7 ± 25.6

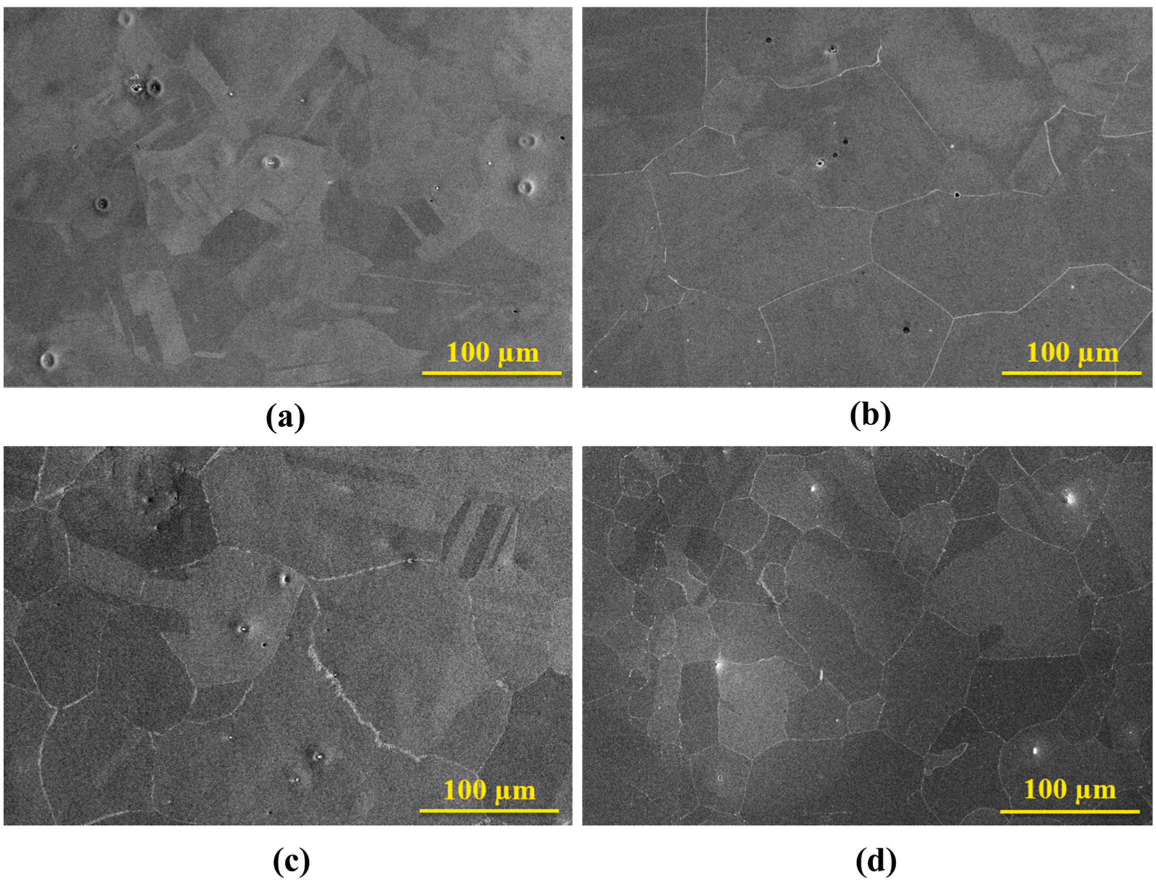

Fig. 1. Scanning electron microscope (SEM) images of (a) SA-00–00, (b) SA-475–10000, (c) SA-550–10000 and (d) SA-700–17 at low magnification.

intergranular carbides on SCC resistance is detrimental when alloy 690 is cold worked. It has been reported that cavities could form along the carbide/matrix interface in cold-worked alloy 690 TT during long-term constant load tests in high temperature water and result in intergranular crack initiation [21–23]. The results from SCC growth rate tests also suggest that intergranular carbides accelerate the crack propagation rate of alloy 690 after cold rolling [21,24–26]. Therefore, the effects of intergranular carbides on the SCC behavior of alloy 690 in PWR primary water are still not clear or well understood as it may depend on other aspects of microstructure and mechanical condition.

In this work, the SCC initiation susceptibilities of alloy 690 samples with different intergranular carbide densities were evaluated through CERT tests in simulated PWR primary water and the carbide effects were systematically explored. The microstructures of degraded grain boundaries were characterized and the mechanism of carbide effects on the SCC initiation behavior is discussed in relation to its roles in the mechanical and chemical processes.

2. Experimental

2.1. Material

The original material block (a commercial heat with 57.6 wt% Ni, 32.7% Cr, 8.64% Fe, 0.25% Mn, 0.315% Al, 0.08% Si and 0.02% C) was solution annealed (SA) at 1100 °C for 1 h and water quenched. To produce different densities of intergranular carbides, several aging treatments were applied to different batches: 10,000 h at 475 °C, 10,000 h at 550 °C, 17 h at 700 °C. The first two aging treatments were used to simulate long term exposure at service temperature and no chemical ordering was found in these samples. Nevertheless, they can be used to accelerate the development of intergranular carbide which occurs slowly at 350 °C. The materials were machined into round tensile bars and designated by the temperature and time of the aging treatments after SA. The gauge length of tensile bar is 20 mm and the diameter is 2 mm. The gauge section was mechanically abraded up to 4000 grit and electropolished for 30 s at 30 V in a solution of 10% (volume fraction) perchloric acid in methanol at − 30 °C. All the samples were cleaned three times alternately with acetone and methanol immediately after

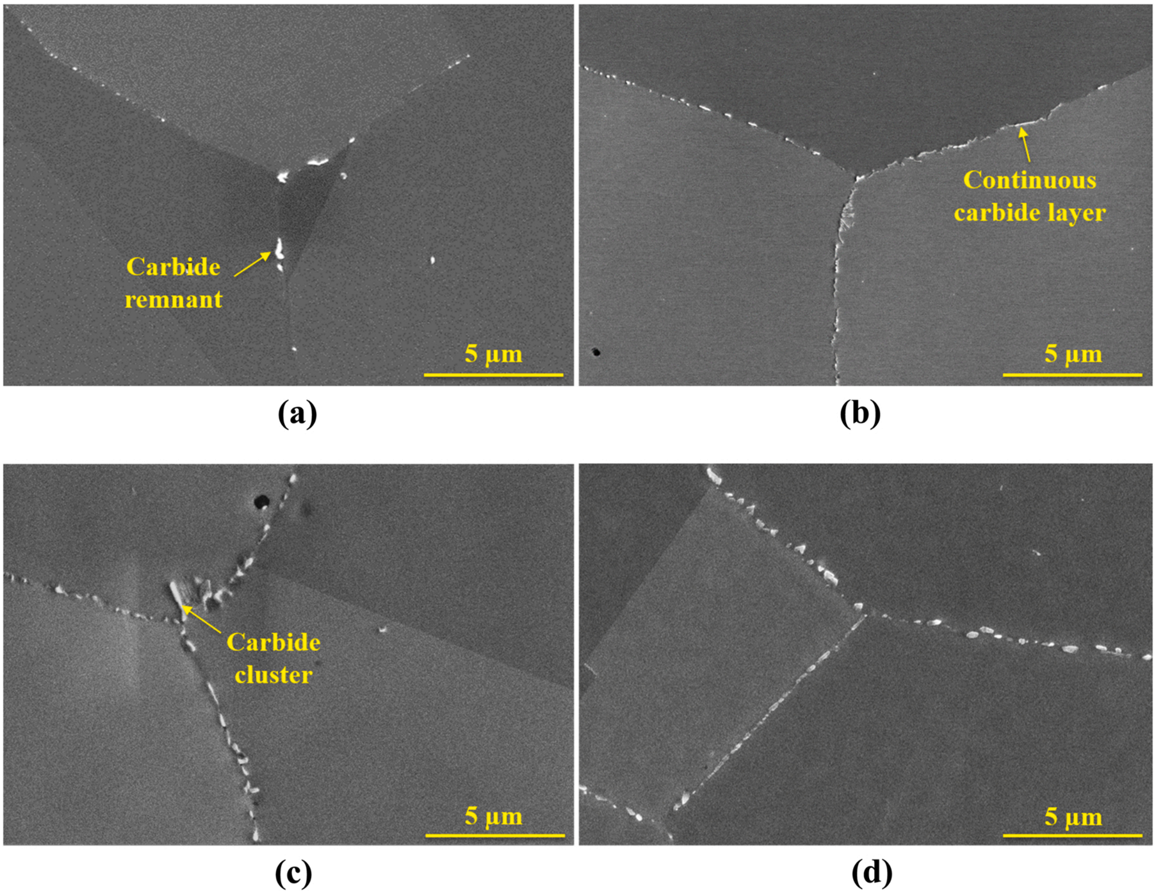

Fig. 2. Scanning electron microscope (SEM) images of (a) SA-00–00, (b) SA-475–10000, (c) SA-550–10000 and (d) SA-700–17 at higher magnification showing the carbide density.

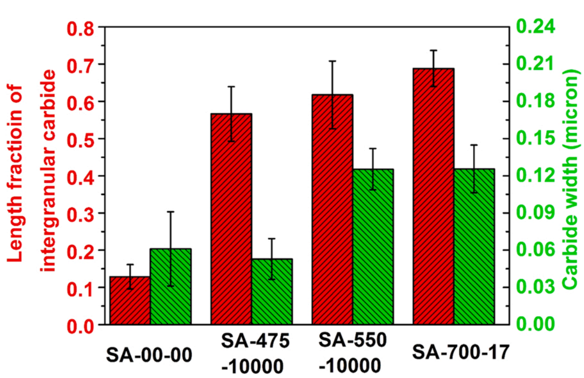

Fig. 3. The length fraction and width of intergranular carbides after different thermal treatments.

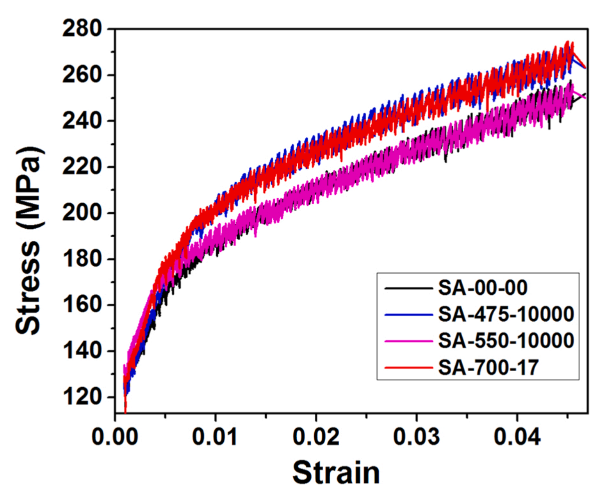

Fig. 4. Stress-strain curves of different samples strained at 1×10^{-8}/s in 360 °C water containing 18 cm^3 (STP) H_2/kg H_2O.

electropolishing. No intergranular surface cracks due to electropolishing were found on the samples. Coupons from each material condition were also prepared to examine the intergranular carbides. The grain sizes measured from SA-00–00, SA-475–10000, SA-550–10000 and SA-700–17 are 72.2 ± 48.3, 91.5 ± 47.2, 97.3 ± 51.6 and 44.2 ± 23.8 μm, respectively. Length coverage and width of carbide were measured for each sample. The length coverage is the length fraction of random high angle grain boundaries covered by carbides. The width of the carbide is the dimension of carbide that is perpendicular to the grain boundary trace. These parameters were measured from images with magnifications ranging from 2000 to 25000 ×. The lengths of grain boundaries for measuring carbide are 420, 194, 580 and 186 μm for SA-00–00, SA-475–10000, SA-550–10000 and SA-700–17 respectively. Standard deviation was calculated to estimate the statistic uncertainty. The continuous carbide cluster was not included in the measurement as the growth of such carbide has extended to the grain matrix significantly.

2.2. *Apparatus and methodology*

The SCC initiation susceptibility was evaluated in 360 °C high purity

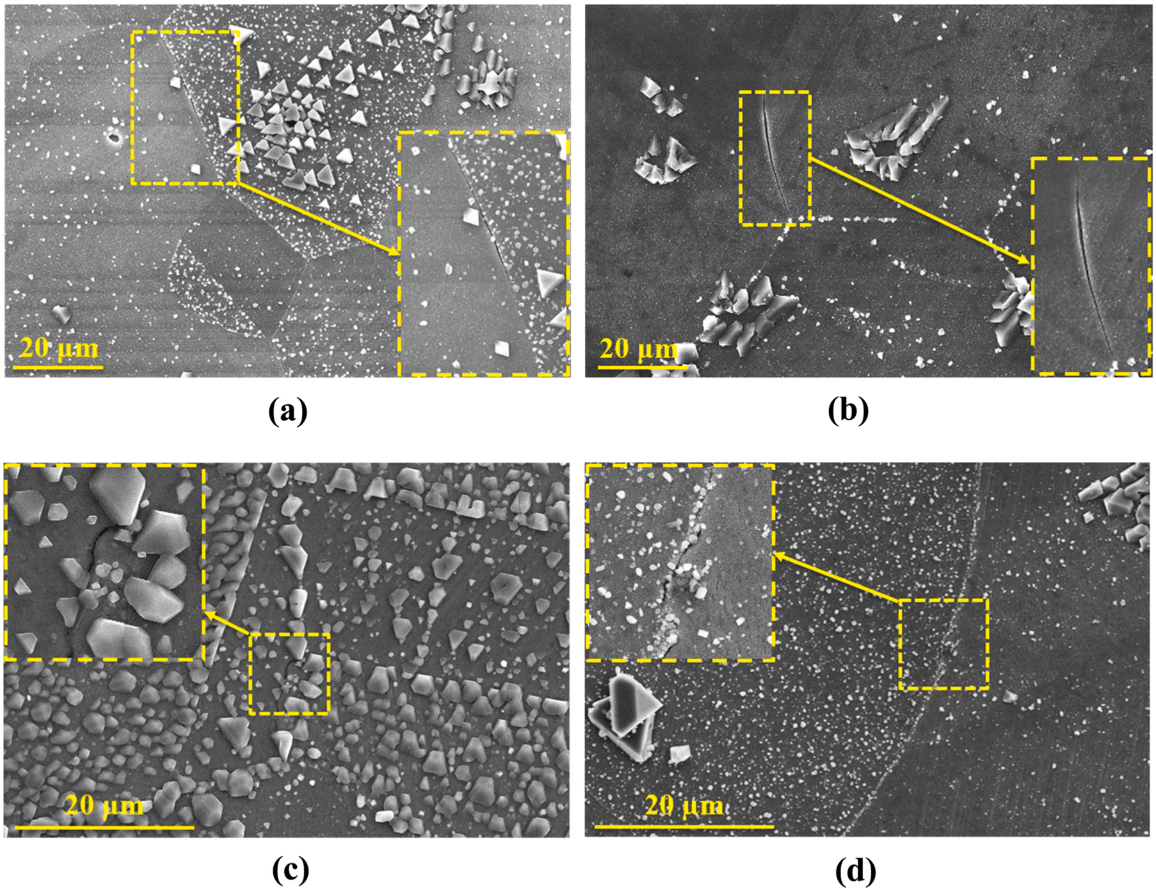

Fig. 5. Intergranular cracks on (a) SA-00–00, (b) SA-475–10000, (c) SA-550–10000 and (d) SA-700–17 after being strained to around 3.4% at 1×10^{-8}/s in 360 °C water containing 18 cm^3 (STP) H_2/kg H_2O. The loading axis is along the horizontal direction.

water using CERT test technique in a refreshed water loop system. The experimental details have been described in our previous work [14,27]. The dissolved hydrogen concentration was controlled at 18 cm^3 (STP) H_2/kg H_2O which provides an electrochemical potential in the NiO stable region (a little above the Ni/NiO boundary). The samples were loaded to just below the yield point at a rate of 1.24×10^{-5}/s once the environment parameters had stabilized for approximately 24 h. Thereafter, the strain rate was lowered to 1×10^{-8}/s. The load and displacement were continuously recorded once every 10 s. All the tensile bars (SA-00–00, SA-475–10000, SA-550–10000 and SA-700–17) were uniformly strained to around 3.4% plastic strain after a total test time of 1391 h. Another pair of samples from SA-00–00 and SA-700–17 was uniformly strained to approximately 1.7% at 1×10^{-8}/s after a total time of 564 h. All the test conditions were summarized in Table 1. The gauge sections of tensile bars were examined using scanning electron microscopy (SEM). More than 40 equally spaced areas on the gauge section were imaged at 1000 ×. The surface intergranular crack lengths were measured and the crack numbers were counted from those images. The images were processed in Photoshop to measure the crack length. Every crack was traced with a single pixel-wide line on a new layer. The amount of pixels for each line was converted to the length of corresponding crack. The average crack length, crack number density (number of cracks per unit area) and crack length density (crack length per unit area) were then calculated to evaluate the susceptibility of SCC initiation as in previous works [2,14,27,28].

The microstructures of some grain boundaries sampled from SA-00–00 and SA-700–17 were further analyzed. The sampled grain boundaries were first examined using SEM in which the loading axis was aligned in the horizontal direction. Cross sections of grain boundaries were made using focused ion beam (FIB) milling on a FEI Helios Nanolab. The FIB cutting procedure has been described in our previous work [4]. The following instruments were used to analyze the FIB lamellas: a JEOL JEM-F200(HR) scanning transmission electron microscope (STEM) which is equipped with two 100 mm^2 energy dispersive spectroscopy (EDS) X-ray detectors and a high angle annular dark-field (HAADF) detector, a Thermo-Fisher Talos F200X equipped with Super-X EDS Detectors and a JEOL 2100 equipped with Octane Super EDS detector. EDS mappings were acquired at 512 × 512 pixels with a dwell time of 40 μs. Each mapping takes about 30 min. EDS line scans were conducted at a step size of 0.75 nm. The dwell time and amplification time for line scan were set to 0.2 and 7.69 μs respectively and the data-processing method was set to Metal Thin.

Digital image correlation (DIC) was used to evaluate the effect of intergranular carbide on the plastic strain distribution near the grain boundary. Two 3 mm-thick alloy 690 plates (a different heat was used here because the previous one was used up) were solution annealed at 1080 °C for 12 min and water quenched. The chemical composition of this alloy heat is: 29.02 wt% Cr, 9.48% Fe, 0.18% Mn, 0.12% Al, 0.12% Si, 0.02% C and balance Ni. One plate was further thermally treated (TT) at 715 °C for 15 h to form intergranular carbides. Microstructure analysis with SEM confirms that the SA sample is almost free of carbide while the TT sample is decorated with dense intergranular carbides. These two plates were machined into 2 mm-thick tensile samples which have a gauge length of 15 mm and a gauge width of 2.5 mm. The studied sample surfaces were mechanically abraded up to 4000 grit and finally electropolished. Both samples were exposed to 320 °C high temperature water containing 30 cc H_2/kg H_2O for 519 h and then strained to ~1.3% at room temperature. Before and after loading, around 30 grain boundaries were selected and imaged in a FEI VERIOS460 SEM with an electron beam current of 80 pA under an accelerating voltage of 15 keV.

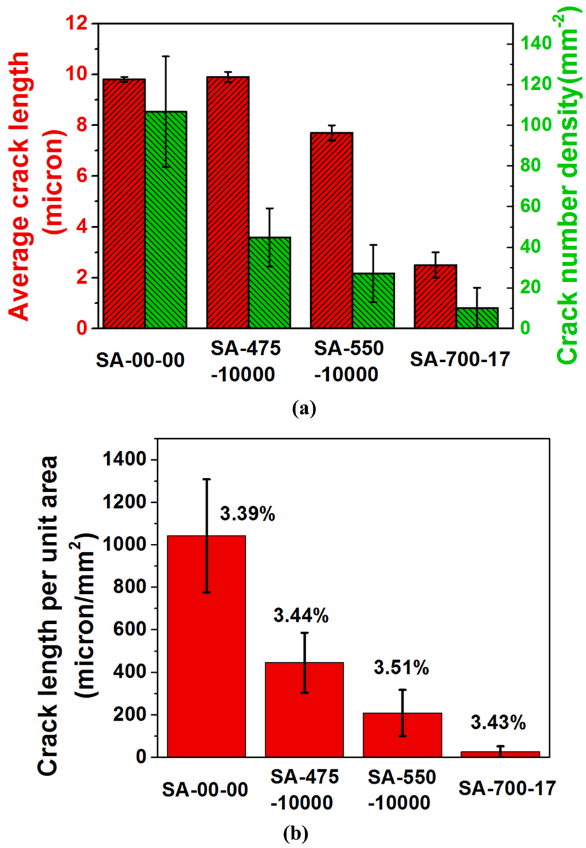

Fig. 6. (a) Average crack length, crack number density (number of cracks per unit area) and (b) crack length density (crack length per unit area) of different samples after constant extension rate tensile (CERT) test in 360 °C water containing 18 cm^3 (STP) H_2/kg H_2O (the applied uniform strain for each sample is listed above the corresponding bar).

As in our previous work [29], the formed surface oxide particles were used as DIC pattern and an open-source 2D DIC software (Ncorr) was used to calculate the local strain distribution [30]. To get a good tradeoff between resolution and noise, the subset radius, subset spacing and strain radius were set to 35, 1 and 10 pixels respectively.

3. Results

Figs. 1 and 2 show the SEM images of the electropolished samples after different aging treatments at low and high magnifications. The precipitates appear brighter than the matrix in the secondary electron imaging mode. As reported in a previous work [9], the grain boundaries on SA-00–00 are almost free of precipitation while some small and scattered precipitates can be still observed along some grain boundaries from the high magnification image (Fig. 2a). Those precipitates are likely remnants of intergranular carbides that were not completely dissolved during solution annealing treatment. Some of the grain boundaries are decorated with a very thin precipitate layer on SA-475–10000 (Fig. 1b). The precipitate layer is semi-continuous, being comprised of small, closely spaced particles (Fig. 2b). Our previous work confirmed that the precipitate is $M_{23}C_6$ [27]. As the aging temperature was increased to 550 °C, the carbide layer thickened (Fig. 1c) and the intergranular carbides increased in size (Fig. 2c). Some of the carbides aggregated into clusters. For SA-700–17, the coverage of carbides on the grain boundary further increased (Fig. 1d) and the intergranular carbides became larger but are still semi-continuous (Fig. 2d). It should be noted that there are some fine-grained regions in SA-700–17 (Fig. 1d), which is probably due to the occurrence of recrystallization in those regions during aging. This explains why the average grain size of this sample is smaller than that of SA-00–00.

The length coverage and width of the intergranular carbides of each sample were measured and the results are plotted in Fig. 3. The length fraction of carbide increases greatly after the aging treatments and then increases slightly with increasing aging temperature. The width of carbide shows noticeable increase only when the aging temperature is higher than 475 °C. The acquired width of carbide shows large statistical uncertainty. The dimension measured from SA-475–10000 is comparable to that from SA-00–00 and the two samples aged at higher temperatures show larger comparable carbide widths.

The stress-strain curves from the CERT test in simulated PWR primary water are plotted in Fig. 4. All the curves are similar and show serrations during plastic deformation. Those serrations are due to dynamic strain aging and have been reported earlier [31,32]. The straining was paused at approximately 3.4% uniform plastic strain. The yield strengths extracted from the stress-strain curves and the final applied strains on the samples are listed in Table 1.

After the CERT tests, the tensile samples were examined in SEM. Intergranular cracks on the gauge section were measured and some examples are given in Fig. 5. The sample surfaces are covered by large spinel oxide particles that are epitaxial with the grain matrixes [33], and the grain boundaries can be readily identified between them. All the samples show intergranular cracks, but to different extents. Clear long intergranular cracks were observed on SA-00–00 and SA-475–10000 (Fig. 5a and b) while only short and shallow cracks appear on SA-550–10000 and SA-700–17 (Fig. 5c and d). The extent of cracking was statistically analyzed as mentioned in Section 2.2, and the results are summarized in Table 1. The data from those samples strained to ~3.4% is plotted in Fig. 6. As shown in Fig. 6a, the average crack length is comparable between SA-00–00 and SA-475–10000 and then decreases for SA-550–1000 and SA-700–17. The crack number density continuously drops in the order of SA-00–00, SA-475–10000, SA-550–1000 and SA-700–17. The crack length density which was used to access the overall SCC initiation susceptibility of materials [2,14,34] is plotted in Fig. 6b. The applied uniform plastic strains were also indicated in the graph. As shown in Fig. 6b, the crack length density decreases significantly in the same order. For the pair strained to ~1.7%, SA-00–00 shows much smaller crack amount than the one strained to ~3.4% and SA-700–17 did not have any detectable cracks (Table 1).

In order to reveal how the intergranular carbide influences the degradation behavior of grain boundary, several grain boundaries were sampled from SA-00–00 and SA-700–17 after the CERT tests. Fig. 7a shows a HAADF image of a grain boundary sampled from SA-00–00 which has been uniformly strained to 1.78% and the corresponding EDS mappings are presented in Fig. 7b. The grain boundary doesn't show sign of cracking from the surface (not shown here) while penetrative intergranular oxide already formed (Fig. 7a). There is a notable grain boundary migration zone beyond the intergranular oxide. The grain boundary migration zone appears brighter than the surrounding matrix due to its higher Ni content [4,8,9]. Non-compact internal oxidation occurs in both grains matrixes, consistent with previous work [33]. The EDS mappings confirm that the migration zone is enriched in Ni while depleted in Cr and Fe (Fig. 7b). Another grain boundary was sampled from SA-00–00 which has been strained to 3.39%. Fig. 7c shows the HAADF image of the grain boundary cross section. The cross section indicates that intergranular oxide, which appears porous, formed within the grain boundary migration zone (Fig. 7c). The corresponding EDS mappings confirm that Ni is enriched while Cr and Fe are depleted in the migration zone (Fig. 7d).

The microstructures of grain boundaries decorated with carbides are significantly different from those of the carbide-free ones. Fig. 8 shows a grain boundary cross section sampled from SA-700–17 which has been strained to 1.63%. Discontinuous particles, which appear darker than the substrate, are observed along the crooked grain boundary (Fig. 8a). Selected area electron diffraction pattern from the intergranular particle confirms that the precipitate is $M_{23}C_6$ type carbide (Inset a1). It should

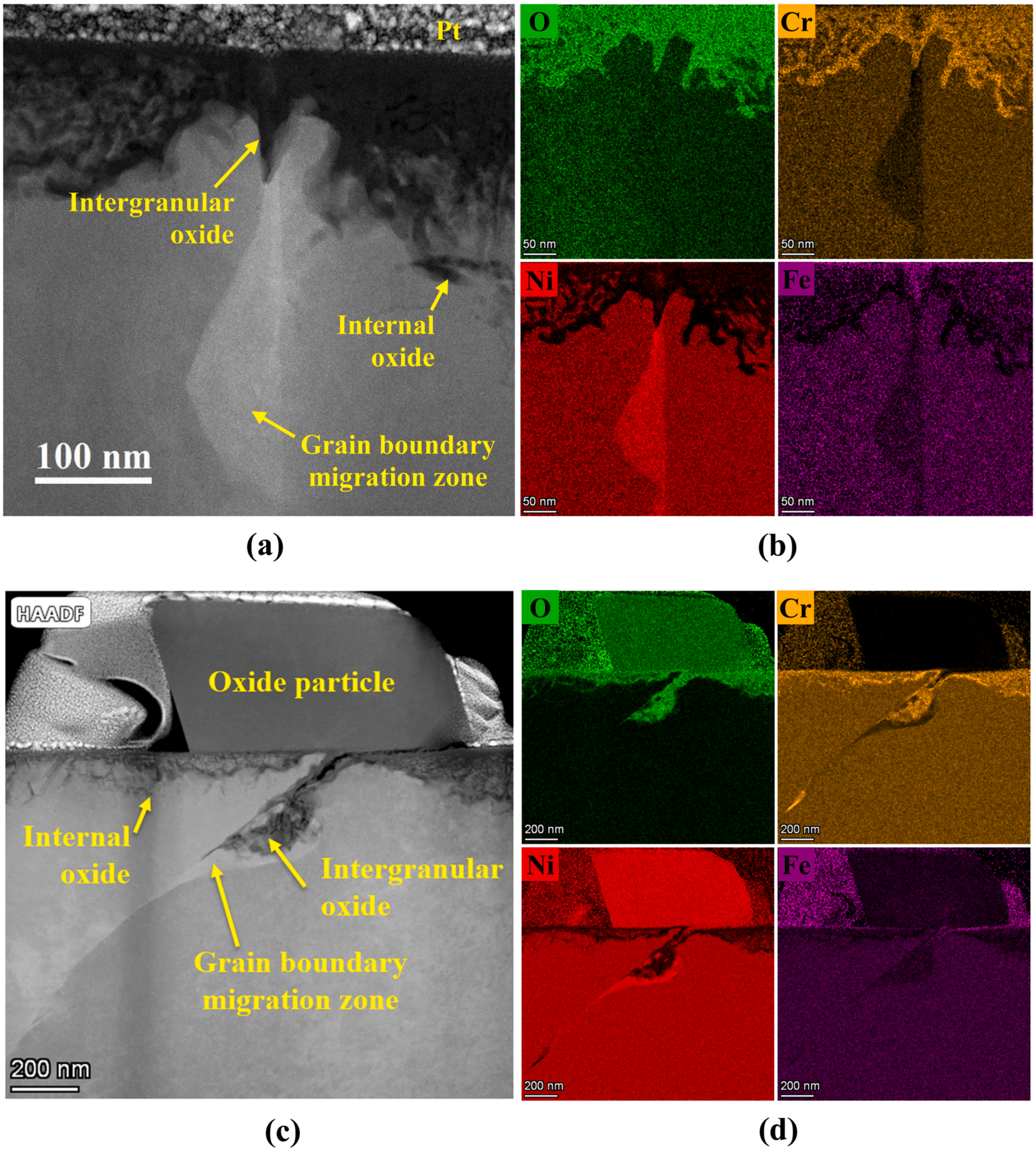

Fig. 7. (a) high angle annular dark-field (HAADF) image of a grain boundary sampled from SA-00–00 after being strained to 1.78% at a rate of 1 × 10^{-8}/s in 360 °C water containing 18 cm^3 (STP) H_2/kg H_2O, (b) EDS mappings of the grain boundary in (a), (c) HAADF image of a grain boundary sampled from SA-00–00 after being strained to 3.39% and (d) EDS mappings of the grain boundary in (c).

be noted that there is a bulge over the grain boundary, as denoted in Fig. 8a. The original matrix surface is represented by a white broken line. The framed area in Fig. 8a is enlarged in Fig. 8b. Between the outer oxide particle and the substrate, there is a very thin layer of compact oxide film beneath which the internal oxidation is minimized (Fig. 8b). Away from the compact oxide layer, internal oxidation penetrates deeper into the matrix. There is a shallow penetrative oxidation zone above the top carbide (Fig. 8b). Two EDS line scans were performed along the two arrows indicated on Fig. 8b. The EDS profile from arrow c shows that there is a Cr-depleted zone (~50 nm wide) in the left grain near the grain boundary (Fig. 8c). The Cr-depleted zone is near the surface and above a carbide. Nevertheless, this is no sign of grain boundary migration from Fig. 8b as there is only one grain boundary trace. The line scan d was performed further down the grain boundary (Fig. 8b) and the profile shows a marginal Cr depletion zone near the grain boundary (Fig. 8d) which typically results from carbide precipitation [35,36].

Another grain boundary was sampled from SA-700–17 which had been strained to 3.43%. Fig. 9a shows the SEM surface image of the sampled area. Both the grain matrixes and boundaries are covered by spinel oxide particles. The oxide particles above the sampled grain boundary can serve as an additional natural protective coating during FIB sample cutting. The HAADF image also shows a thin compact oxide layer and a bulge above the grain boundary with discrete carbides along the grain boundary (Fig. 9b). Internal oxide forms in the matrix away from the grain boundary. A shallow penetrative oxidation zone also forms above the top carbide. Bright field image was taken to check if the grain boundary had migrated sideways. It clearly indicates that the grain boundary is basically straight with no sign of migration (Fig. 9c). EDS mapping on this grain boundary is shown in Fig. 10. The HAADF image

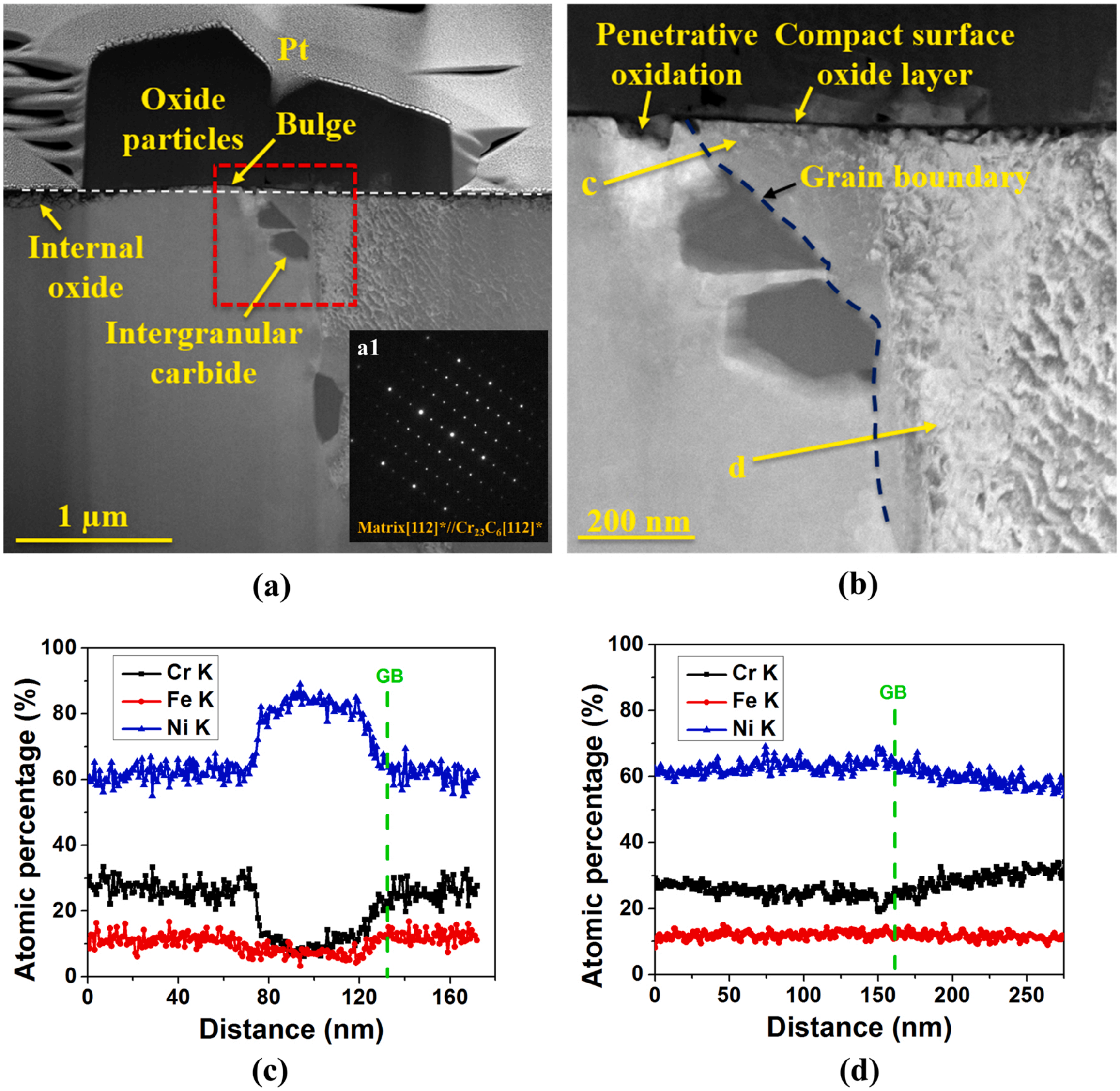

Fig. 8. (a) HAADF image of the cross section of grain boundary sampled from SA-700–17 after being strained to 1.63% at a rate of 1×10^{-8}/s in 360 °C water containing 18 cm^3 (STP) H_2/kg H_2O (inset a1 is a selected area electron diffraction pattern from the intergranular particle), (b) enlarged HAADF image from the framed area in (a), (c, d) energy dispersive spectroscopy (EDS) profiles along the arrows in (b).

in Fig. 10a was flipped over compared to Fig. 9b. The compact oxide layer over the grain boundary and the internal oxide are enriched in Cr (Fig. 10e) and depleted in Fe and Ni (Fig. 10c and d), indicating that those oxides are basically chromia. The previous works also suggest that the oxide above the grain boundary [1] and the internal oxide in the grain matrix of alloy 690 [33] are mainly composed of chromia. The spinel oxide particle formed above the surface is rich in Fe and contains some Ni (Fig. 10c and d), consistent with the previous works which reported that those spinel particles are $NiFe_2O_4$ [33,37,38]. Interestingly, Cr rich oxide forms around the top carbide, as indicated by O and Cr mappings (Fig. 10b and e). Besides, the top carbide shows sign of decomposition and is partially replaced by Ni-rich metal (Fig. 10d and e). Although the grain boundary did not migrate, there is Cr depletion between the top three carbides which becomes narrower as it moves downwards (Fig. 10e). Meanwhile, Ni is enriched in this zone (Fig. 10d). The Ni-enriched narrow zone seems to go through the second carbide because this carbide does not extend through the whole sample thickness and the Ni enriched zone overlaps the carbide.

Fig. 11 shows the XX strain distributions from DIC measurement on alloy 690 tensile samples with and without intergranular carbides. The tensile direction is along the X axis. Some of the grain boundaries sampled from the SA sample exhibit apparent slip band transmission across the grain boundary (Fig. 11a and b), indicating the transmission of dislocation. On the contrary, such feature was not observed on the TT sample. Interestingly, some grain boundaries from the TT sample clearly show minimization of strain near the boundary (Fig. 11c and d), suggesting that the movement of dislocation was suppressed as it gets close to the boundary.

4. Discussion

SCC is a complex form of environmental degradation which involves both mechanical and chemical processes. The results presented here clearly show that the resistance to SCC initiation can be significantly affected by the precipitation of intergranular carbides. The effect of carbides on the susceptibility to SCC initiation will be evaluated first and then discussed in relation to its roles in both mechanical and chemical processes.

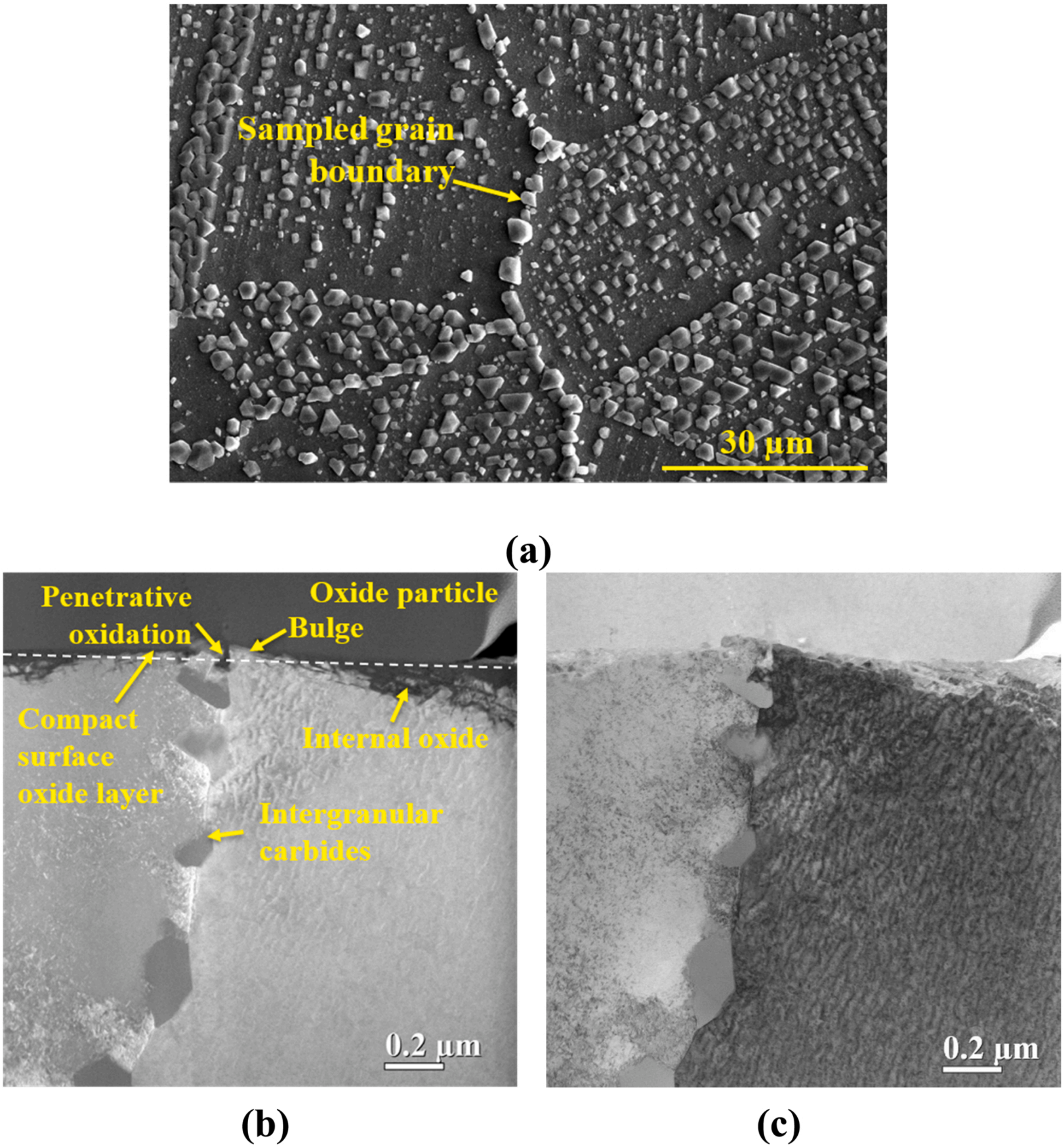

Fig. 9. (a) SEM image, (b) HAADF and (c) bright field images of a grain boundary sampled from SA-700–17 after being strained to 3.43% at a rate of 1×10^{-8}/s in 360 °C water containing 18 cm^3 (STP) H_2/kg H_2O.

4.1. Effect of intergranular carbide on SCC initiation susceptibility

Fig. 6 clearly shows that the crack number density and crack length density after the CERT test decreases continuously in the order of SA-00–00, SA-475–10000, SA-550–1000 and SA-700–17. The average crack length also shows the same trend except that it is comparable between SA-00–00 and SA-475–10000. Thus, the resistance to SCC initiation increases continuously in the order of SA-00–00, SA-475–10000, SA-550–1000 and SA-700–17.

The improved resistance to SCC initiation should be closely related to the microstructure changes induced by the aging treatment. Although the grain size increases a little after the aging treatments at 475 and 550 °C (Fig. 1), the effect of grain size on the SCC resistance is not significant and the evolution of grain size doesn't coincide with the change of resistance to SCC initiation. The remaining major change in the microstructure is the intergranular carbide density. The different combinations of aging temperature and time used in this work produced a broad range of carbide distribution. From Fig. 3, both the length fraction and the width of intergranular carbide were changed by the aging treatments. The length fraction of carbides barely changes and the carbide width increases from SA-475–10000 to SA-550–10000, while the length fraction increases and the width doesn't change much from SA-550–10000 to SA-70–17. Given that the crack length density continuously decreases from SA-00–00 to SA-700–17 (Fig. 6b), it seems that increase in either of the two parameters can improve the SCC resistance. An increasing length fraction of intergranular carbide can enhance the resistance to SCC initiation because a higher fraction of grain boundary is decorated with carbides. The beneficial effect of growing carbide size is probably because a larger size can enhance the role of carbides in the mechanical and chemical processes of SCC which will be discussed below. While cracking susceptibility decreases with increasing carbide fraction and width, the figure of merit of effective carbide coverage (equal to the grain boundary length fraction times the width of intergranular carbide) is introduced to include the effects of both.

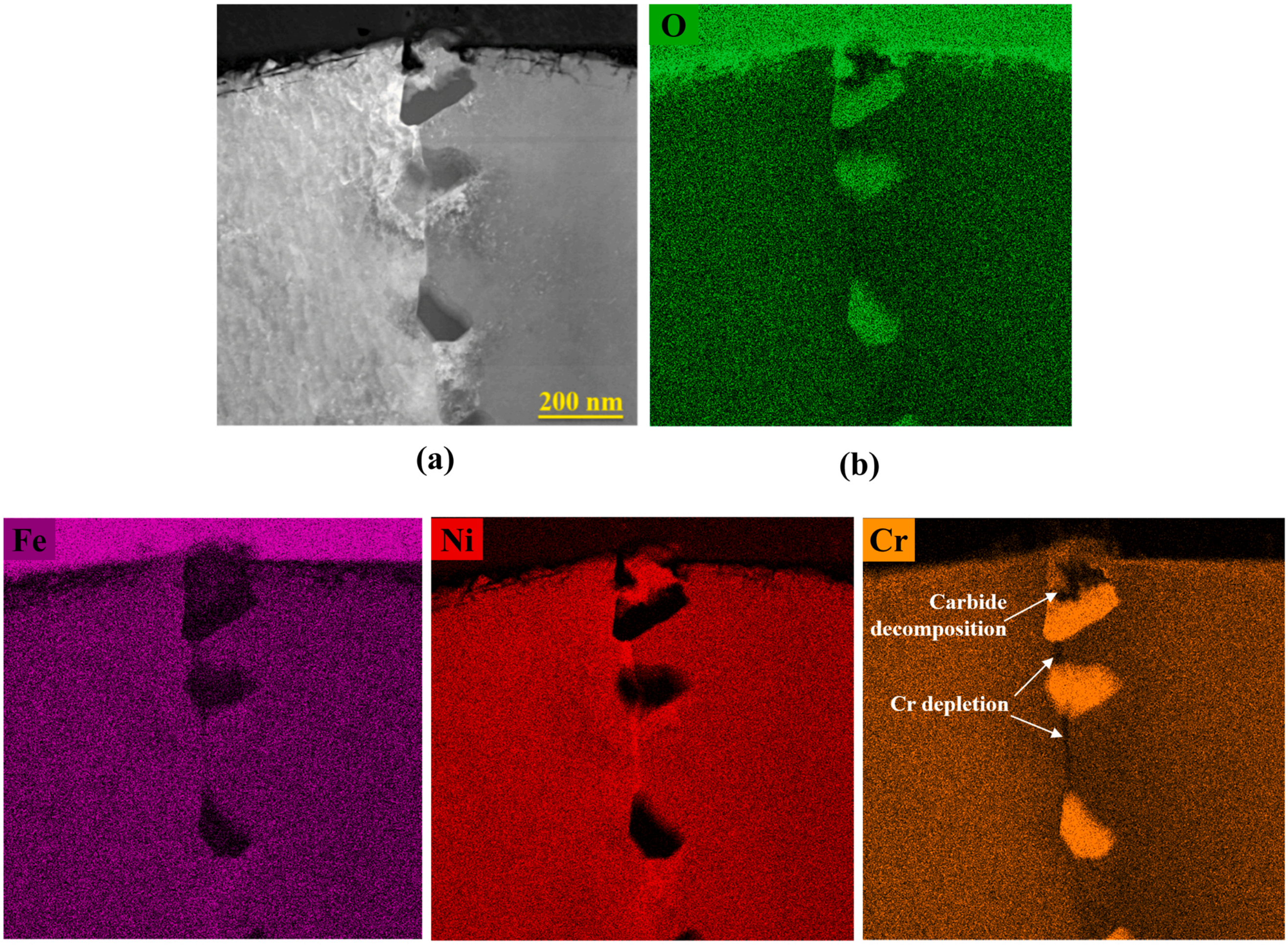

(a) (b) (c) (d) (e)

Fig. 10. (a) HAADF and (b-e) the corresponding EDS mapping of the grain boundary sampled from SA-700–17 after being strained to 3.43% at a rate of 1×10^{-8}/s in 360 °C water containing 18 cm^3 (STP) H_2/kg H_2O.

Interestingly, the effective carbide coverage increases continuously in the order of SA-00–00, SA-475–10000, SA-550–1000 and SA-700–17, which is very consistent with the continuous improvement in the resistance to SCC initiation. The change of crack length density was plotted versus the effective carbide coverage in Fig. 12. It clearly shows that the crack length density drops significantly as the effective carbide coverage increases. The mitigation effects on SCC initiation from the intergranular carbide formed at aging temperature of 700 °C or above have also been reported from previous CERT tests on cold worked alloy 690 [14] as well as alloy 600 [10,11,39,40]. Thus, the SCC initiation resistance of alloy 690 in hydrogenated high temperature water can be significantly enhanced as the effective coverage of intergranular carbide increases, regardless of the aging temperature.

4.2. Role of intergranular carbide in the mechanical process of SCC initiation

Intergranular carbides have a significant effect on the mechanical behavior of material and hence affects the SCC initiation susceptibility during the CERT test. Carbides are strong obstacles to dislocation movement. Thus, the dislocations pile up near the intergranular carbides during deformation, as evidenced by the high resolution electron backscatter diffraction on a nickel base superalloy with carbide inclusions [41] and transmission Kikuchi diffraction on cold-worked alloy 600 [20]. The high geometrically necessary dislocation density near the carbide is linked to the large strain gradient [41]. Abuzaid et al. [42] have also shown that there exists an inverse relation between the magnitude of residual Burgers vector of dislocations and the plastic strain across the grain boundary. The DIC results shown in Fig. 11 reveal that the slip transmission was suppressed in the sample with intergranular carbides. As the dislocation movement is significantly impeded by the intergranular carbide, the apparent plastic strain near the grain boundary is smaller than in the rest of the grain matrix (Fig. 11c and d). That is why there is a bulge over most of the grain boundaries (6 out of 7) sampled from SA-700–17 (as shown in Figs. 8a and 9b) while the solution annealed sample does not show such feature (Fig. 7). The limited strain near the grain boundary may be closely related to the enhanced SCC initiation resistance of materials with intergranular carbides. It has been reported that alloy 690 tends to form a compact oxide layer over the random high angle grain boundary [1–6] and breach of such oxide layer is an essential precursor in SCC initiation process of this alloy [7, 8]. Local plastic strain is probably the driving force for the breach of the oxide layer formed over grain boundary as the oxide film is normally brittle and can be readily fractured during plastic deformation. As the plastic strain near the grain boundary is suppressed by the intergranular carbides, the surface oxide film formed above the boundary would not be easily breached and the resistance to SCC initiation is enhanced. In addition, the dislocations accumulated near the intergranular carbide could accelerate the outward diffusion of Cr and promote the formation of protective oxide film, which may partly explain the formation of a

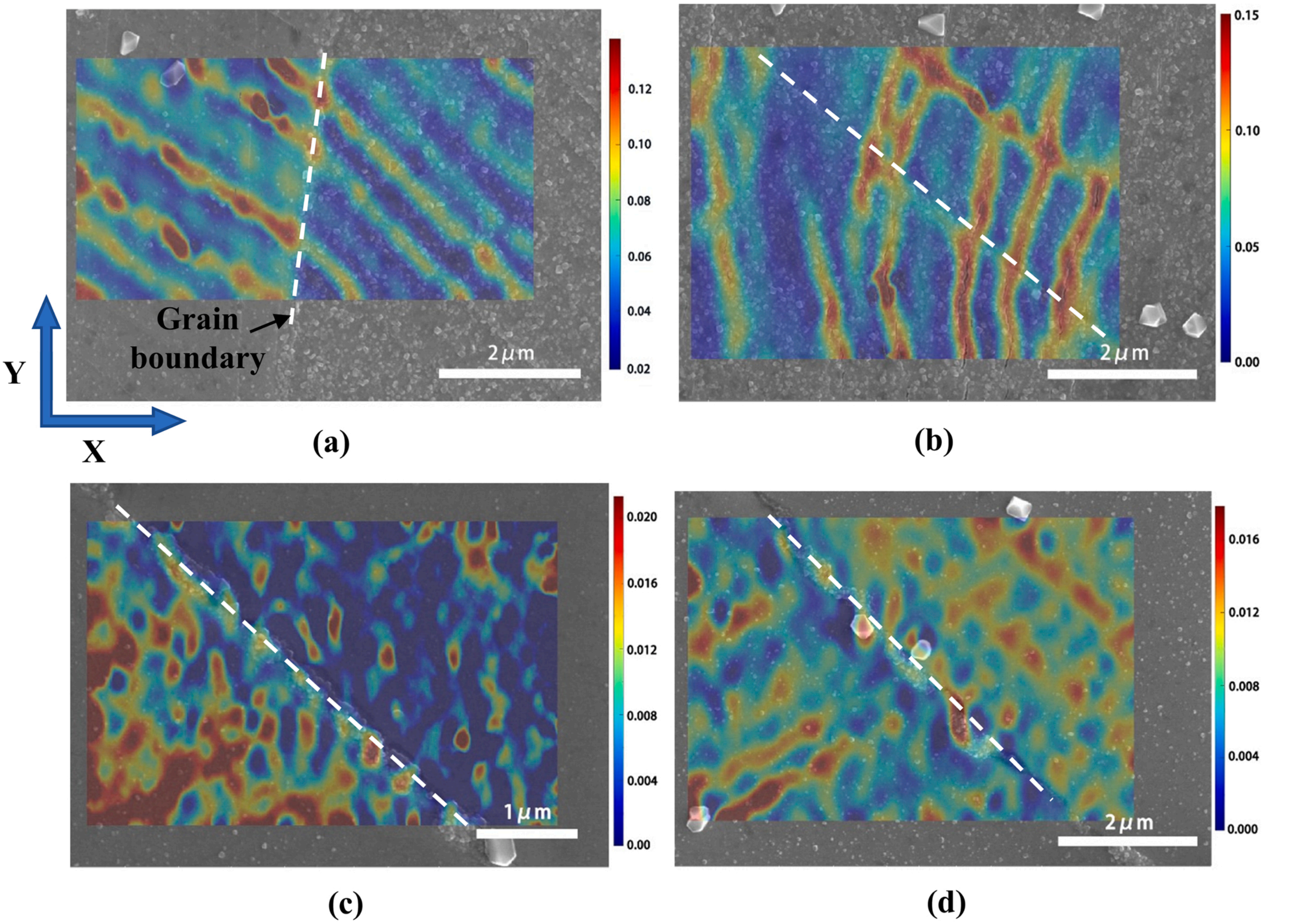

Fig. 11. XX strain distribution from DIC measurement on (a, b) alloy 690SA and (c, d) alloy 690TT after ~1.3% plastic strain at room temperature. The tensile direction is along the X axis.

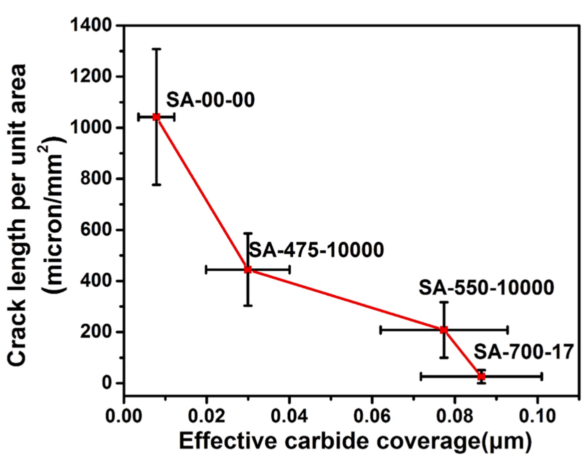

Fig. 12. Change of crack length density as a function of effective carbide coverage.

compact oxide layer on a wide range of area above the grain boundary for SA-700–17 (Fig. 8b).

The beneficial effect of carbides on SCC of alloy 690 may be only limited to the initiation stage and highly dependent on the mechanical condition. The detrimental effect of carbide on the resistance to SCC propagation of cold worked alloy 690 has been well recognized [24–26] and is thought to be closely related to the highly concentrated local residual strain near the carbide [43]. It should be noted that there is no diffusion barrier layer during SCC propagation and oxygen can penetrate fast along the interface with accumulated dislocations. In addition, formation of creep cavities around the carbides beyond the crack tip has been observed in cold worked alloy 690 [21]. The constant load tests on cold-worked alloy 690 also reveal that grain boundary carbides can promote the formation of cavities [22,23] along the grain boundary inside the material. As summarized in a recent review by Arioka [44], carbides act as nucleation sites for cavity formation in cold worked materials that can lead to IG crack formation. Therefore, the effect of intergranular carbides on the resistance to IG cracking is highly dependent on the mechanical condition of the alloy. There is probably a deformation tolerance level below which the intergranular carbide is beneficial to the SCC resistance. Beyond this level, the local accumulated residual strain and concentrated stress near the carbide would be high enough to promote the formation of cavities along the carbide/matrix interface under tensile stress or induce fast ingress of oxygen through the highly defective region when there is no diffusion barrier.

4.3. *Role of intergranular carbides in the chemical process of SCC initiation*

The intergranular carbide also plays a significant role in the chemical process during the SCC initiation of alloy 690. It has been reported that grain boundary migration, which is induced by the outward diffusion of Cr along the grain boundary, is an important phenomenon during the SCC of solution-annealed alloy 690 in simulated PWR primary water [1, 4,8,9]. The grain boundary migration zone is also clearly observed on grain boundaries sampled from SA-00–00 (Fig. 7). Interestingly, grain boundary migration was inhibited after the precipitation of intergranular carbides as indicated in Figs. 8 and 9. From the EDS mapping in Fig. 10e, the sharp Cr depletion zone along the grain boundary is narrow and limited to the space between the top three carbides. Beyond the 3rd carbide, the Cr depletion resulting from carbide precipitation gets much milder. The sharp Cr depletion zone narrows down along the grain boundary and vanishes beyond the 3rd carbide, suggesting that Cr depletion near the surface was not caused by carbide precipitation, but by the outward diffusion of Cr during oxidation. Therefore, the outward diffusion of Cr along the grain boundary is greatly suppressed by the intergranular carbide, thus diminishing grain boundary migration. A similar result has also been reported in alloy 600 when exposed to 480 °C hydrogenated steam [19]. The ability to form a Cr-rich oxide film over the grain boundary in simulated PWR primary water renders alloy 690 more resistant to SCC initiation than alloy 600 [1,4,7,8]. As Cr is needed for the formation of such protective oxide film, fast diffusion of Cr can promote the formation of Cr-rich oxide film and mitigate SCC initiation. Previous works also indicate that the resistance to crack initiation is related to the efficiency of Cr transport along grain boundary [9,45]. Therefore, at the initial stage of SCC initiation of alloy 690, the intergranular carbide reduces the Cr diffusion along grain boundary which may retard the formation of Cr-rich oxide film over the boundary.

Although the supply of Cr via grain boundary diffusion is retarded by intergranular carbides, the carbide itself can serve as a Cr source. As indicated in Fig. 10e, the top intergranular carbide shows signs of decomposition from the surface. The Cr depletion zone above the top carbide in Fig. 8b should also result from decomposition of this carbide. The Cr from the decomposed part probably participates in the formation of a protective surface oxide film. Previous work [18] on the oxidation of alloy 600 in 480 °C hydrogenated steam has revealed that the intergranular carbide in alloy 600 was susceptible to decomposition and the released Cr promoted the formation of a protective Cr-rich surface oxide. Our recent work [46] also suggests that the intergranular carbide in alloy 690 is the major Cr source for forming chromia at the interface between carbide and matrix. Thus, in the simulated PWR primary water, the intergranular carbide exposed to the environment is subject to decomposition and provides additional Cr for the formation of Cr-rich oxide over grain boundary in alloy 690. This additional Cr source could replenish the diminished Cr supply from grain boundary diffusion.

The intergranular carbide can still mitigate the intergranular oxidation of alloy 690 even after the surface oxide film over grain boundary is breached. Figs. 8b and 9b show much shallower penetrative oxidation above the carbide than the intergranular oxidation depth in Fig. 7a and c. The Cr-depleted grain boundary migration zone in alloy 690 is susceptible to penetrative oxidation (Fig. 7), as reported in previous works [8,9]. Given that the intergranular carbide can significantly suppress the boundary migration and serve as Cr source, the intergranular oxidation should be mitigated and the process of SCC would be retarded. It has also been reported that the intergranular carbide could effectively reduce the intergranular oxide penetration depth in alloy 600 under both simulated PWR primary water [17] and 480 °C hydrogenated steam [19].

5. Conclusion

The effect of intergranular carbide on the stress corrosion crack (SCC) initiation behavior of alloy 690 aged at different temperatures in simulated PWR primary water was systematically investigated using constant extension rate tensile (CERT) test. It was observed that the crack length density decreases significantly with increasing effective carbide coverage, irrespective of the aging temperature.

The enhanced resistance to SCC initiation by intergranular carbides arises from its roles in both the mechanical and chemical processes of SCC. In the mechanical process, the intergranular carbide suppresses the apparent plastic strain near the grain boundary, thus decreasing the driving force for the breach of the surface oxide film. The accumulated dislocations near the carbide may also promote the diffusion of Cr to the surface. In the chemical process, the intergranular carbide effectively retards the diffusion of Cr along the grain boundary and greatly diminishes grain boundary migration. More importantly, the carbide near the surface is subject to decomposition and provides additional Cr for the formation of protective oxide film. Consequently, the intergranular carbide promotes the formation of protective surface oxide film and mitigates intergranular oxidation when the surface oxide film is breached.

CRediT authorship contribution statement

Wenjun Kuang: Conceptualization, Data curation, Funding acquisition, Investigation, Methodology, Project administration, Supervision, Draft writing and revision **Xingyu Feng:** Data curation, Methodology, Visualization. **Han Yue:** Methodology, Software. **Gary S. Was:** Funding acquisition, Investigation; Project administration, Draft reviewing. **Xianchao Hao:** Resources, Investigation.

Declaration of Competing Interest

The authors declare that they have no known competing financial interests or personal relationships that could have appeared to influence the work reported in this paper.

Data availability

The raw/processed data required to reproduce these findings cannot be shared at this time as the data also forms part of an ongoing study.

Acknowledgements

The authors gratefully acknowledge Young Suk Kim and Sung Soo Kim from Korea Atomic Energy Research Institute for providing the materials for this study and the financial supports of National Natural Science Foundation of China (No. 51971172), Development Program of the Ministry of Science and Technology of China (No. 2019YFA0209900) and the Young Talent Support Plan of Xi’an Jiaotong University. The authors thank Dr. Chao Li at Instrument Analysis Center of Xi’an Jiaotong University for his assistance with STEM and EDS analysis.

References

[1] M.J. Olszta, D.K. Schreiber, M.B. Toloczko, S.M. BruemmerAlloy 690 surface nanostructures during exposure to PWR primary water and potential influence on stress corrosion crack initiation, in: The 16th international conference on environmental degradation of materials in nuclear power systems-water reactors, Asheville, North Carolina, USA, 2013.
[2] T. Moss, G.S. Was, Accelerated stress corrosion crack initiation of alloys 600 and 690 in hydrogenated supercritical water, Metall. Mater. Trans. A 48 (2017) 1613–1628.
[3] S.Y. Persaud, S. Ramamurthy, R.C. Newman, Internal oxidation of alloy 690 in hydrogenated steam, Corros. Sci. 90 (2015) 606–613.
[4] W. Kuang, G.S. Was, The effect of grain boundary structure on the intergranular degradation behavior of solution annealed alloy 690 in high temperature, hydrogenated water, Acta Mater. 182 (2020) 120–130.
[5] Y.S. Lim, D.J. Kim, S.W. Kim, S.S. Hwang, H.P. Kim, Characterization of internal and intergranular oxidation in Alloy 690 exposed to simulated PWR primary water and its implications with regard to stress corrosion cracking, Mater. Charact. 157 (2019), 109922.
[6] L. Volpe, M.G. Burke, F. Scenini, Oxidation behaviour of solution-annealed and thermally-treated Alloy 690 in low pressure H2-Steam, Corros. Sci. 167 (2020), 108514.
[7] T. Moss, W. Kuang, G.S. Was, Stress corrosion crack initiation in alloy 690 in high temperature water, Curr. Opin. Solid State Mater. Sci. 22 (2018) 16–25.
[8] W. Kuang, G.S. Was, A high-resolution characterization of the initiation of stress corrosion crack in Alloy 690 in simulated pressurized water reactor primary water, Corros. Sci. 163 (2020), 108243.

[9] W. Kuang, M. Song, G.S. Was, Insights into the stress corrosion cracking of solution annealed alloy 690 in simulated pressurized water reactor primary water under dynamic straining, Acta Mater. 151 (2018) 321–333.
[10] T.S. Bulischeck, D.V. Rooyen, Stress corrosion cracking of alloy 600 using the constant strain rate test, Corrosion 37 (1981) 597–607.
[11] B. Alexandreanu, B. Capell, G.S. Was, Combined effect of special grain boundaries and grain boundary carbides on IGSCC of Ni–16Cr–9Fe–xC alloys, Mater. Sci. Eng.: A 300 (2001) 94–104.
[12] K. Norring, J. Engstrom, P. Norberg, Intergranular Stress Corrosion Cracking in Steam Generator Tubing. Testing of Alloy 690 and Alloy 600 Tubes., in: Proc. 3rd Int. Symp. Environmental Degradation of Materials in Nuclear Power Systems — Water Reactors, Traverse city, Michigan, 1987.
[13] J.M. Sarver, J.R. Crum, W.L. Mankins, Carbide precipitation and the effect of thermal treatments on the SCC behavior of Inconel Alloy 690, in: Proceedings of the third international symposium on Environmental Degradation of Materials in Nuclear Power Systems-Water Reactors, The Metallurgical Society, Traverse City, Michigan, 1987.
[14] W. Kuang, G.S. Was, The effects of grain boundary carbide density and strain rate on the stress corrosion cracking behavior of cold rolled Alloy 690, Corros. Sci. 97 (2015) 107–114.
[15] S.M. Bruemmer, L.A. Charlot, C.H. Henager, Microstructure and microdeformation effects on IGSCC of alloy 600 steam generator tubing, Corrosion 44 (1988) 782–788.
[16] S.Y. Persaud, A. Korinek, J. Huang, G.A. Botton, R.C. Newman, Internal oxidation of Alloy 600 exposed to hydrogenated steam and the beneficial effects of thermal treatment, Corros. Sci. 86 (2014) 108–122.
[17] F.O. M. Gaslain, H.T. Le, C. Duhamel, C. Guerre, P. Laghoutaris, The role of intergranular chromium carbides on intergranular oxidation of nickel based alloys in pressurized water reactors primary water, IOP Conference Series: Materials Science and Engineering. 109 (2016) 012004.
[18] G. Bertali, F. Scenini, M.G. Burke, The intergranular oxidation susceptibility of thermally–treated Alloy 600, Corros. Sci. 114 (2017) 112–122.
[19] B. Langelier, S.Y. Persaud, A. Korinek, T. Casagrande, R.C. Newman, G.A. Botton, Effects of boundary migration and pinning particles on intergranular oxidation revealed by 2D and 3D analytical electron microscopy, Acta Mater. 131 (2017) 280–295.
[20] Z. Shen, J. Liu, K. Arioka, S. Lozano-Perez, On the role of intergranular carbides on improving the stress corrosion cracking resistance in a cold-worked alloy 600, J. Nucl. Mater. 514 (2019) 50–55.
[21] K. Arioka, T. Yamada, T. Miyamoto, T. Terachi, Dependence of stress corrosion cracking of alloy 690 on Temperature, Cold Work, and Carbide Precipitation—Role of Diffusion of Vacancies at Crack Tips, Corrosion 67 (2011) 035006-1–035006-18.
[22] K. Arioka, T. Terachi, Degradation of Alloy 690 after relatively short times, Corrosion 72 (2016) 1252–1268.
[23] Z. Zhai, M. Toloczko, K. Kruska, S. Bruemmer, Precursor evolution and stress corrosion cracking initiation of cold-worked alloy 690 in simulated pressurized water reactor primary water, Corrosion 73 (2017) 1224–1236.
[24] M.B. Toloczko, M.J. Olszta, S.M. Bruemmer, One dimentional cold rolling effects on stress corrosion crack growth in Alloy 690 tubing and plate materials, in: 15th Int. Conf. on Environmental Degradation of Materials in Nuclear Power Systems-water reactors, Colorado Springs, Colorado, USA, 2011.
[25] P.L. Andresen, M.M. Morra, K. Ahluwalia, Effect of deformation temperature, orientation and carbides on SCC of Alloy 690, in: 16th international conference on environmental degradation of materials in nuclear power systems-water reactors, Asheville, North Carolina, USA, 2013.
[26] K. Chen, J. Wang, Z. Shen, D. Du, X. Guo, L. Zhang, P.L. Andresen, Effect of intergranular carbides on the cracking behavior of cold worked alloy 690 in subcritical and supercritical water, Corros. Sci. (2019), 108313.
[27] W. Kuang, G.S. Was, C. Miller, M. Kaufman, T. Alam, B. Gwalani, R. Banerjee, The effect of cold rolling on grain boundary structure and stress corrosion cracking susceptibility of twins in alloy 690 in simulated PWR primary water environment, Corros. Sci. 130 (2018) 126–137.
[28] W. Kuang, C. Miller, M. Kaufman, T. Alam, B. Gwalani, R. Banerjee, Effects of cold work and aging treatments on the microstructure and stress corrosion cracking initiation behavior of solution annealed alloy 690, in: 17th Int. Conf. on Environmental Degradation of Materials in Nuclear Power Systems-water reactors, Ottawa, Ontario, Canada, 2015.
[29] W. Kuang, H. Yue, X. Feng, B. Yang, C. Guo, A novel test technique for the mechanistic study of initiation of environmentally assisted cracking on a Ni–30Cr–10Fe alloy in simulated pressurized water reactor primary water, Scr. Mater. 189 (2020) 122–128.
[30] J. Blaber, B. Adair, A. Antoniou, Ncorr: open-source 2D digital image correlation matlab software, Exp. Mech. 55 (2015) 1105–1122.
[31] W. Kuang, G.S. Was, The effects of strain rate and carbon concentration on the dynamic strain aging of cold rolled Ni-based alloy in high temperature water, Scr. Mater. 107 (2015) 107–110.
[32] T. Moss, G. Was, Dynamic strain aging of nickel-base alloys 800H and 690, Metall. Mater. Trans. A 43 (2012) 3428–3432.
[33] W. Kuang, M. Song, P. Wang, G.S. Was, The oxidation of alloy 690 in simulated pressurized water reactor primary water, Corros. Sci. 126 (2017) 227–237.
[34] S. Teysseyre, G.S. Was, Stress corrosion cracking of austenitic alloys in supercritical water, Corrosion 62 (2006) 1100–1116.
[35] K. Chen, J. Wang, D. Du, X. Guo, L. Zhang, Characterizing the effects of in-situ sensitization on stress corrosion cracking of austenitic steels in supercritical water, Scr. Mater. 158 (2019) 66–70.
[36] J.J. Kai, G.P. Yu, C.H. Tsai, M.N. Liu, S.C. Yao, The effects of heat treatment on the chromium depletion, precipitate evolution, and corrosion resistance of INCONEL alloy 690, Metall. Trans. A 20 (1989) 2057–2067.
[37] W. Kuang, X. Wu, E.-H. Han, J. Rao, The mechanism of oxide film formation on Alloy 690 in oxygenated high temperature water, Corros. Sci. 53 (2011) 3853–3860.
[38] W. Kuang, X. Wu, E.-H. Han, Influence of dissolved oxygen concentration on the oxide film formed on Alloy 690 in high temperature water, Corros. Sci. 69 (2013) 197–204.
[39] J.L. Hertzberg, G.S. Was, Isolation of carbon and grain boundary carbide effects on the creep and intergranular stress corrosion cracking behavior of Ni-16Cr-9Fe-xC alloys in 360 °C primary water, Metall. Mater. Trans. A 29 (1998) 1035–1046.
[40] G.S. Was, K. Lian, Role of carbides in stress corrosion cracking resistance of alloy 600 and controlled-purity Ni-16% Cr-9% Fe in primary water at 360°C, Corrosion 54 (1998) 675–688.
[41] P.S. Karamched, A.J. Wilkinson, High resolution electron back-scatter diffraction analysis of thermally and mechanically induced strains near carbide inclusions in a superalloy, Acta Mater. 59 (2011) 263–272.
[42] W.Z. Abuzaid, M.D. Sangid, J.D. Carroll, H. Sehitoglu, J. Lambros, Slip transfer and plastic strain accumulation across grain boundaries in Hastelloy X, J. Mech. Phys. Solids 60 (2012) 1201–1220.
[43] S.M. Bruemmer, M.J. Olszta, M.B. Toloczko, L.E. Thomas, Linking grain boundary microstructure to stress corrosion cracking of cold-rolled alloy 690 in pressurized water reactor primary water, Corrosion 69 (2012) 953–963.
[44] K. Arioka, Role of cavity formation on long-term stress corrosion cracking initiation: a review, Corrosion 76 (2019) 142–175.
[45] M.-R. He, D.C. Johnson, G.S. Was, I.M. Robertson, The role of grain boundary microchemistry in irradiation-assisted stress corrosion cracking of a Fe-13Cr-15Ni alloy, Acta Mater. 138 (2017) 61–71.
[46] W. Kuang, M. Song, X. Feng, Insight into the acceleration in oxidation kinetics ahead of stress corrosion crack of alloy 690 in simulated PWR primary water, Corros. Sci. 176 (2020), 108943.